5

The $H \rightarrow WW^* \rightarrow \mu^{\pm}\nu_{\mu}\tau^{\mp}_{had}\bar{\nu}_{\tau}$ final state

5.1 Motivation

In order to achieve maximal sensitivity to the SM Higgs signal, it is crucial to explore all the possible final states. This chapter will discuss about the feasibility studies done in one such channel, $\mu + \tau_{had}$ final state. The $H \rightarrow WW^* \rightarrow \mu^{\pm}\nu_{\mu}\tau^{\mp}_{had}\bar{\nu}_{\tau}$ final state can enhance the sensitivity of the $H \rightarrow WW^* \rightarrow \ell^{+}\nu\ell^{-}\nu$ final state by adding channels in which τ leptons decay hadronically. This analysis uses a smaller dataset and different multivariate techniques as used in the di-electron analysis already presented in this thesis. Analysis with final states containing τ leptons are generally difficult because of the problems related with τ reconstruction and identification. When the W bosons decays into τ leptons, the subsequent tau decay can either take place via an electron, muon or hadrons. The events where the tau leptons decays further into electrons or muons are mostly selected by the $H \rightarrow WW^* \rightarrow e^{\pm}\nu\mu^{\mp}\nu$ analysis. Among the rest of the final states, the $\mu + \tau_{had}$ final state with the μ arising from one of the W boson decays and the other W boson decaying via a τ lepton further decaying hadronically (τ_{had}), offers the highest efficiency. The hadronic decay modes of τ separates this final state from other leptonic final states and also brings in additional signal events. The τ identification algorithms are also sensitive to some of those electrons, which are likely to be missed in the $H \rightarrow WW^* \rightarrow e^{\pm}\nu\mu^{\mp}\nu$ analysis and can therefore be recovered via this final state. The next sections will discuss the methods and techniques used for this analysis.

5.2 Data Sample

The data used for this analysis was collected between June 2006 and September 2008 by DØ detector, covering a small part of the complete RunIIb data sample. The analysis uses dataset which requires at least one reconstructed muon in each event. The integrated luminosity for this sample was found to be 1.62 fb^{-1}.

5.3 Triggers

The data for the $\mu + \tau_{had}$ final state is only triggered via muon triggers. In the analysis, we require data to pass through at least one of the nine dedicated high-p_T single muon trigger.

Tag and Probe method is the method used to measure the muon trigger efficiencies. We

select a low-background sample of $Z \to \mu\mu$ data events by requiring the di-muon invariant mass to be consistent with the Z mass and chooses one of the two muons to be the "tag" muon. This muon must then fire some other trigger that is unbiased with respect to the other (probe) muon. The other muon is the probe muon, and one tests whether or not there are trigger objects that pass the trigger requirements overlapping this offline muon, and then parametrize the fraction of muons with overlapping trigger objects (the efficiency) as a function of one or more kinematic variables. In this analysis, we parametrize the efficiency as a function of muon p_T, η and ϕ. The efficiency thus measured are then applied to all MC samples [72, 73].

5.4 Monte Carlo for Signal and Backgrounds

All signal and background MC samples used in the analysis were generated in NLO using Pythia MC generator [46] followed by a detailed GEANT based simulation of DØ detector. The events are generated at a center of mass energy of $\sqrt{s} = 1.96\ TeV$ assuming a top quark mass of $m_t = 172.5\ GeV/c^2$ and using the CTEQ6L1 parton distribution functions (PDFs) [50].

The main background processes for the analysis are Z decay in muon and tau final states, diboson production and electroweak $W + jet/\gamma$ production, $t\bar{t}$ and the multijet production. The SM cross-sections for the background processes are listed in Appendix D.

The cross section for $Z/\gamma^* \to ll$ processes is calculated with CTEQ6M1 PDFs as $\sigma(Z/\gamma \to ll) = \sigma_{LO} \times K_{QCD}(Q^2)$ according to [58, 59]. The LO cross section, σ_{LO}, uses LO PDF while the K factor, K_{QCD}, is calculated with respect to NNLO with NLO PDF as a function of the momentum transfer, Q^2. The $W + \text{jets}/\gamma$ cross section is calculated with NNLO corrections and CTEQ6M1 as listed in [58]. The $t\bar{t}$ cross section is calculated at NNLO in [74] and the WW, ZZ and WZ cross sections are calculated in [57] with MCFM using CTEQ6M1 PDFs. The background contribution of multijet production has been estimated from data and is discussed in section 5.6.

The signal cross sections have been calculated for different Higgs boson masses using the branching ratios as listed in [75]. Various Higgs boson production channels are contributing to the total signal. The main production channel is the so called gluon-fusion $gg \to H \to WW^* \to \ell\nu\ell\nu$. The second largest Higgs boson production takes place at the Tevatron via the vector boson-fusion (VBF). Minor additional signal contributions are coming from ZH and WH production.

5.5 Object Identification

5.5.1 Muon Selection

The muon identification used in this analysis is based on the following selection criteria (Variable definition can be seen in section 3.5:

- At least one muon in the event.

- Muon $p_T \geq 15\ GeV/c$
- Central track matched muon.
- NSeg≥ 3
- DCA $> 0.2cm$ ($> 0.02cm$) for track with no (≥ 1) SMT hits.
- $|\eta_{det}| < 1.6$
- $\Delta z(PV, \mu) \geq 1.5cm$, where PV is the primary vertex.
- Track Isolation: $I_{trk} < 2.5GeV$
- Calorimeter Isolation: $I_{cal} < 2.5GeV$
- $\chi^2_{trk} < 4$
- A veto on cosmic muons is applied to suppress muons from cosmic radiation. The standard cosmic ray veto requires A and BC scintillator times $|t| < 10$ ns.

5.5.2 Tau Selection

A hadronically decaying tau is characterized by a narrow isolated jet into three standard types, which are distinguished by their detector signatures as follows:

- Type I: Calorimeter cluster, with one associated track and no EM subcluster. This corresponds mainly to the decay $\tau^{\pm} \to \pi^{\pm}\nu$.
- Type II: Calorimeter cluster, with one associated track and at least one EM subcluster. This corresponds mainly to the decay $\tau^{\pm} \to \pi^{\pm}\pi^0\nu(\rho\nu)$.
- Type III: Calorimeter cluster, with two or three associated tracks, with or without EM subclusters. This corresponds mainly to the decays $\tau^{\pm} \to \pi^{\pm}\pi^{\pm}\pi^{\mp}\pi^0\nu(3-prong)$.

For the present analysis, only tau type I and II are used. Due to very high background and very small signal sensitivity, tau type III has been neglected.

- The transverse momentum p_T of a τ candidate must be greater than 15 GeV/c for each tau type.
- The track p_T, for the track associated with the τ candidate is required to be greater than 7 GeV/c for τ type I and $p_T > 5\ GeV/c$ for τ type II.
- A Neural Network(NN) trained for each tau type, is used in the analysis to separate real taus from those that originate from jet fakes. In addition, the NN for τ type I is trained separately for events within the ICD region.

- The energy of hadronic taus is corrected by providing correct calorimeter EM scale. This correction leads to a better MC/data agreement in the E^{cal}/P^{trk} as well as the invariant mass of the $\mu-\tau$ pair. The $\not\!\!E_{\mathrm{T}}$ is recomputed after the tau energy is corrected.
- Taus matching jets and muons (selected in the analysis) within a cone of radius 0.5 are removed from the event. This ensures that the lepton in the event once identified as tau is not double counted as a jet or a muon.

5.5.3 Jets

As already discussed the hadronization process produces a large number of colorless hadrons that appear in the detector as a collimated "jet" of hadronic particles and deposit a cluster of energy in the calorimeter, typically the shape of a cone. The reconstruction, identification and calibration of jets are already explained in the section 3.7. Jets have to fulfill the following quality criteria:

- Jet p_T more than 20 GeV/c
- $|\eta| < 2.5$
- $CoarseHadronicFraction$ is required to be < 0.4
- $L1Confirmation$ is required to be > 0.5
- $0.05 < EMfraction < 0.95$

5.6 Mulitjet Background

The multijet events are the main source of instrumental background where jets are misidentified as fake leptons. This background is estimated directly from data using a method similar to what was described earlier 4.5.1. To get an estimate of the multijet contribution, a like-sign (SS) enriched sample of lepton fakes is required. All the selection criteria described in the section 5.5.1, 5.5.2 and 5.5.3 are applied, except that the muon candidate is required to fail the isolation criteria. Additionally an upper limit for the calorimeter and track isolation is also applied.

$$\begin{gathered} 2.5\ GeV < I_{cal} < 7.0 GeV. \\ I_{trk} < 7.0\ GeV \end{gathered}$$

where I_{cal} is the calorimeter isolation for muon candidates and I_{trk} is the track isolation for the same. For the tau objects the NN output has to be $0.3 < NN < 0.7$. By inverting muon and tau quality cuts in the SS case an enriched sample of multijet and W+jets events with almost no $Z/\gamma^* + \text{jet}$ contribution is selected. This sample is referred to as "fake sample".

This sample of SS leptons is used to normalize the multijet contribution in the data sample. The number of SS events $N^{\pm\pm}_{multi}$, corresponding to the multi-jet contribution in the

τ type I - 0.231
τ type II - 0.346

Table 5.1: The normalization factors for each τ type.

SS signal sample, is computed from the excess of like-sign events $N^{\pm\pm}_{data}$ above the expected contribution $N^{\pm\pm}_{MC}$ from all SM backgrounds:

$$N^{\pm\pm}_{multi} = N^{\pm\pm}_{data} - N^{\pm\pm}_{MC}. \tag{5.1}$$

Then, the normalization factor for the multijet sample is defined as

$$f_{multi} = \frac{N^{\pm\pm}_{multi}}{N^{\pm\pm}_{fake}(p_T)} \tag{5.2}$$

here $N^{\pm\pm}_{fake}$ corresponds to the number of the like-sign events in the fake sample. The number of multi-jet events in the unlike-sign signal sample $N^{\pm\mp}_{multi}$ is determined from the number of unlike-sign fake events $N^{\pm\mp}_{fake}(p_T)$ using the formula

$$N^{\pm\mp}_{multi} = f_{multi} \cdot N^{\pm\mp}_{fake}(p_T) \tag{5.3}$$

The normalization factor is evaluated as a function of τ p_T, but as one can see in the Fig. 5.1, that the p_T parametrization for the SS sample appear to be flat, hence only one correction factor is derived for the full p_T range. These normalization factors are calculated for each tau type and are summarized in Table 5.1.

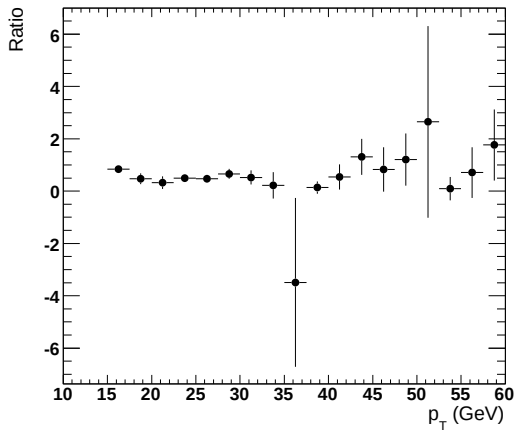

Figure 5.1: The normalization function for multijet background for RunIIb as a function of the transverse momenta of the τ_{II} which appears to be flat. Hence only one normalization factor is taken to be p_T independent.

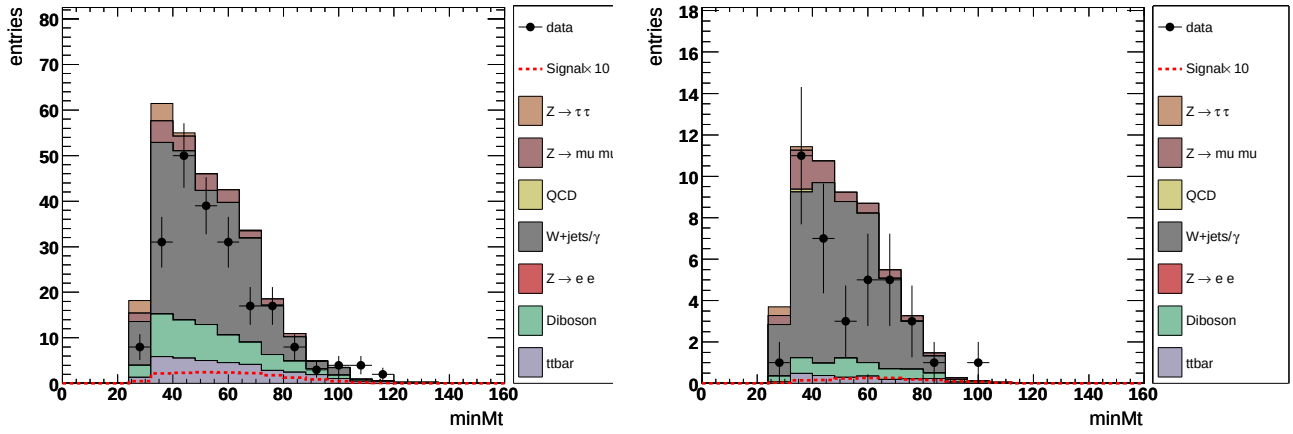

Figure 5.2: Distribution of the minimum transverse mass in the enriched region for $\mu+\tau_{II}$ (left) and $\mu+\tau_{I}$ (right) before any correction is applied at pre-selection level for data (points) and sum of all backgrounds (filled histograms). The expected signal, multiplied by a factor of 10, for a $160 GeV/c^2$ SM Higgs is also shown.

5.7 Electroweak Reference sample

The Pythia MC used to estimate the electroweak $W+\text{jets}/\gamma$ background does not reproduce the collision data well. The $W+\text{jets}/\gamma$ enriched sample in data is therefore used and is selected by having oppositely charged leptons and $M_t^{min} > 30 GeV/c^2$. This background is thus enhanced in this enriched region as seen in Fig. 5.2. A correction is then derived by looking at the excess of events in data over all SM background expectation in this enriched sample. The cross section of $W+\text{jets}/\gamma$ events is then modified to reproduce the data. The correction factors thus needed are determined to be close to 0.55 for both tau type I and II. The effect of these correction factors for both tau types can be seen in the Fig. 5.3.

5.8 Veto on Events selected by $H \to WW^* \to \mu e$ analysis

In order to stay orthogonal to the $H \to WW^* \to e^{\pm}\nu\mu^{\mp}\nu$ analysis, a veto is applied. This is done for each Higgs boson mass point. All the events selected in this analysis fail the $H \to WW^* \to e^{\pm}\nu\mu^{\mp}\nu$ selection. Selection cuts are applied on only the events that pass the veto. The veto is implemented in such a way to maintain the sensitivity of this analysis and as well as select the events that could not make into the $H \to WW^* \to e^{\pm}\nu\mu^{\mp}\nu$ final selection due to tighter lepton criteria imposed in the selection.

5.9 Event Selection

Two classes of selection requirements are used in the analysis. Firstly, kinematic cuts on object and event properties are applied as explained in section 5.9.1. Secondly, a multivariate discriminant i.e, an Artificial Neural Network (ANN or NN), described in section 5.10, is used

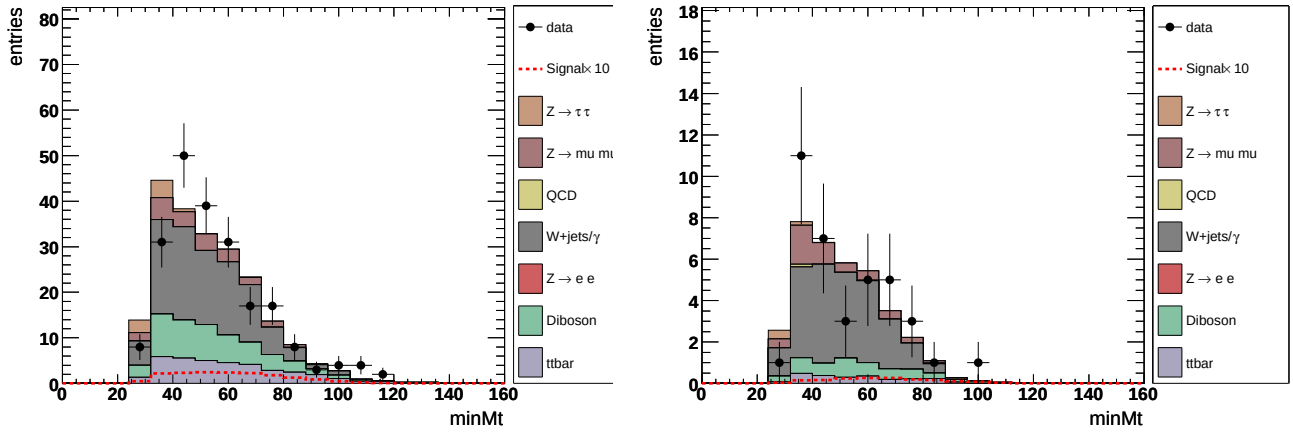

Figure 5.3: Distribution of the minimum transverse mass in the enriched region for $\mu + \tau_{lI}$ (left) and $\mu + \tau_{l}$ (right) after the corrections are applied (right) at pre-selection level for data (points) and sum of all backgrounds (filled histograms). The expected signal, multiplied by a factor of 10, for a 160 GeV/c^2 SM Higgs is also shown.

to separate the signal from background events. The background at the pre-selection level is dominated by $Z/\gamma^* + \text{jet}$ and multijet events. The background composition changes as selection cuts are applied. The kinematic distributions at pre-selection and after various cuts for both τ types can be seen in the following sections.

5.9.1 Selection Requirements using kinematic cuts

The analysis is performed for 5 different Higgs mass points using a mass range of $m_H = 120 - 200\ GeV/c^2$ in steps of 20 GeV/c^2. In order to gain maximal sensitivity only loose kinematical cuts are applied.

Cut 0	pre-selection	lepton ID, leptons with opposite charge and $p_T^{\mu} > 15\ GeV/c$ and $p_T^{\tau} > 15\ GeV/c$ Single Muon Trigger OR, $M_{\mu\tau} > 15\ GeV/c^2$
Cut 1	Missing Transverse Energy $\not\!\!E_{\mathrm{T}}$	> 20.0 GeV
Cut 2	$M_{min}^{T}\ (l, \not\!\!E_{\mathrm{T}})$	> 20.0 GeV
Cut 3	$\Delta\phi(\mu, \tau)$	< 2.5

Table 5.2: Summary of selection criteria applied in the analysis

The number of events selected after each selection requirement for data, expected signal and the various background contributions are listed in Table 5.5 and 5.6.

The following list illustrates the effect of the various selection requirements:

- Cut 0 (pre-selection) :The two leptons are required to be of opposite charge, not

matched to each other [$\Delta R \geq 0.5$], and must have $p_T x > 15$ GeV/c for both muon and tau. Additionally the invariant mass $M_{\mu\tau}$ is required to exceed 15 GeV/c^2.

- Cut 1: A cut on the missing transverse energy in the event $\not\!\!E_{\rm T} > 20$ GeV is applied to suppress the large $Z/\gamma^* + \text{jet}$ background and to reject multijet events.
- Cut 2: A cut on the minimal transverse mass of M^T_{min} $(l, \not\!\!E_{\rm T}) > 20$ GeV between the leptons and the missing transverse energy suppresses further contributions from $Z/\gamma^* + \text{jet}$ and $W + \text{jets}/\gamma$ backgrounds.
- Cut 3: A selection requirement on the opening angle between the two selected electrons of $\Delta\phi(\mu, \tau) < 2.5$ is placed. This removes most of the remaining $Z/\gamma^* + \text{jet}$ events while being largely independent of the particular Higgs mass kinematics. The reduction of the $Z/\gamma^* + \text{jet}$ background prior to the training of the NN results in a more balanced contribution of the sample of events used for the NN training between the different backgrounds. This reduces the weight assigned to the mass variable relative to the other variables used in the NN discriminant and an overall better rejection of all the backgrounds.

Table 5.2 summarizes these selection cuts. Figs. 5.4 and 5.5 presents the distributions of minimal transverse mass and invariant mass at pre-selection and after applying one of the above mentioned selection cuts for the $\mu + \tau_{II}$ final state while Figs. 5.6 and 5.7 presents the same for $\mu + \tau_I$ final state.

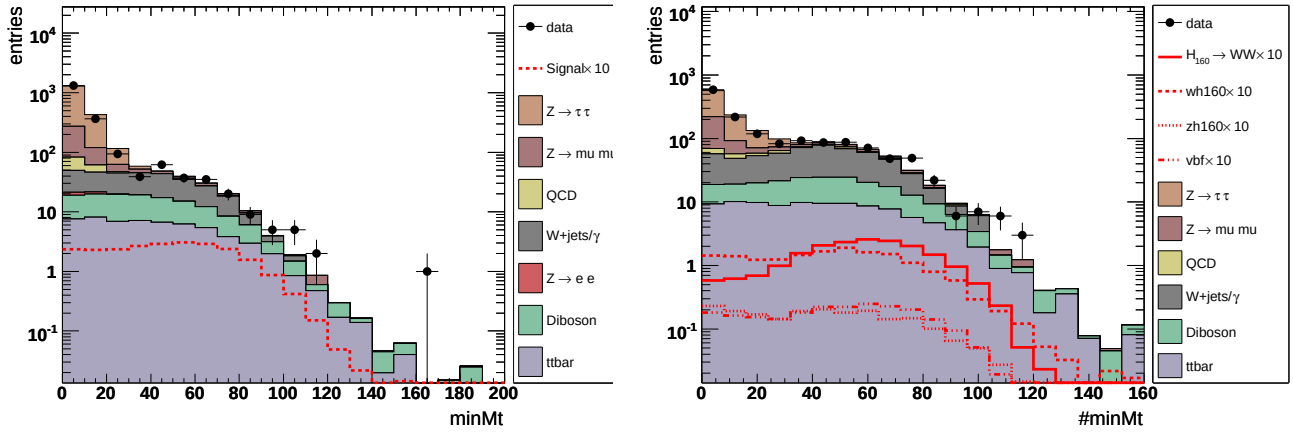

Figure 5.4: Distribution of the minimal transverse mass after pre-selection (left) and after the $\not\!\!E_{\rm T}$ cut (Cut 1) is applied (right) for $\mu + \tau_{II}$. The expected signal, multiplied by a factor of 10, for a 160 GeV/c^2 SM Higgs is also shown.

Distributions of the $\Delta\phi(\mu, \tau)$ and $\not\!\!E_{\rm T}$ after applying various selection criteria for the $\mu+\tau_{II}$ and $\mu + \tau_I$ final states are shown in Figs. 5.8, 5.9.

5.9.2 Data/MC Yields for the various Higgs masses

The expected signal yields for various SM Higgs boson masses studied for $\mu + \tau_{II}$ final state is shown in Table 5.3 and for $\mu + \tau_I$ final state in Table 5.4. From these tables one can

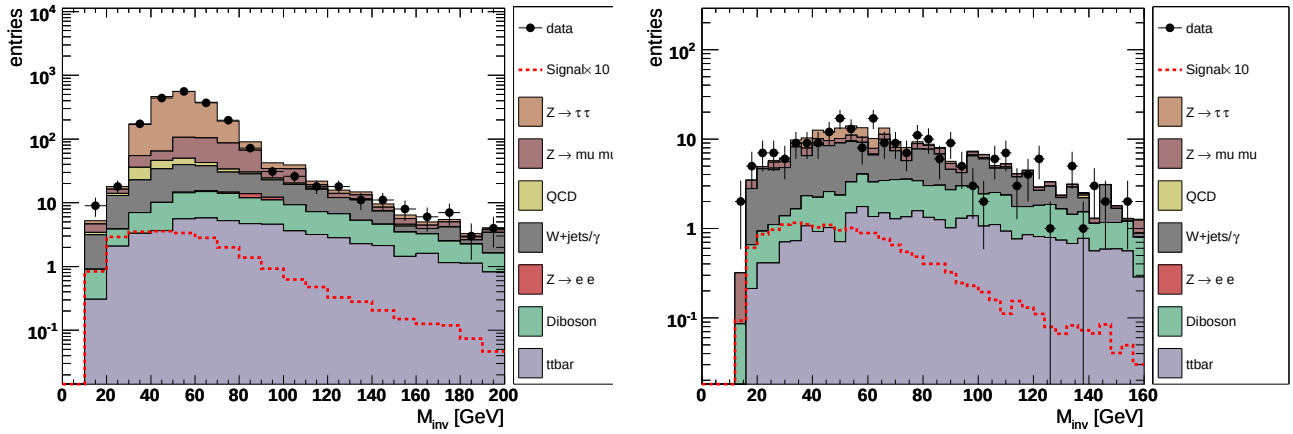

Figure 5.5: Distribution of the invariant mass after pre-selection (left) and after the minimal transverse cut (Cut 2) is applied (right) for $\mu + \tau_{II}$. The expected signal, multiplied by a factor of 10, for a 160 GeV/c^2 SM Higgs is also shown.

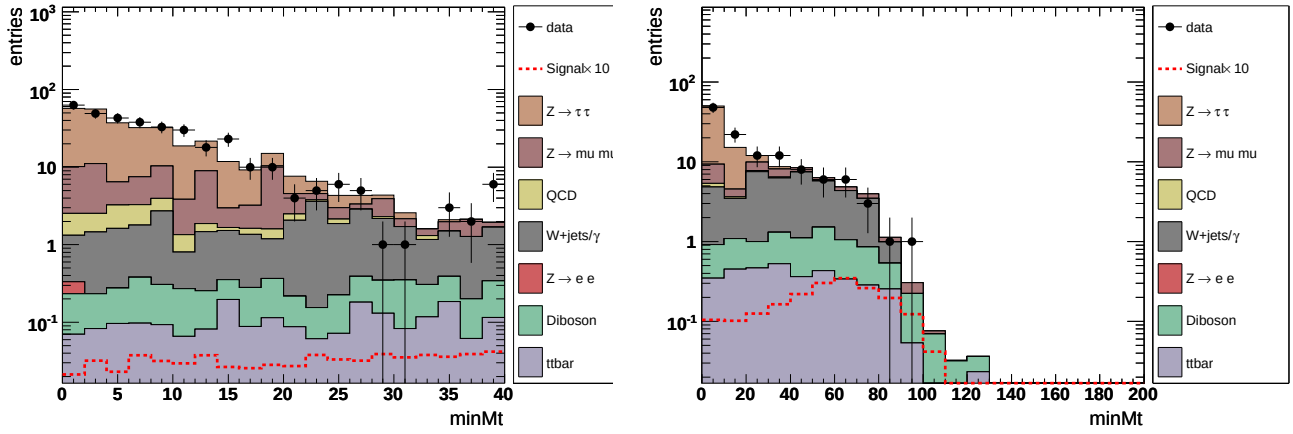

Figure 5.6: Distribution of the minimal transverse mass after pre-selection (left) and after the $\not{E}_{\mathrm{T}}$ cut (Cut 1) is applied (right) for $\mu + \tau_I$ final state. The expected signal, multiplied by a factor of 10, for a 160 GeV/c^2 SM Higgs is also shown.

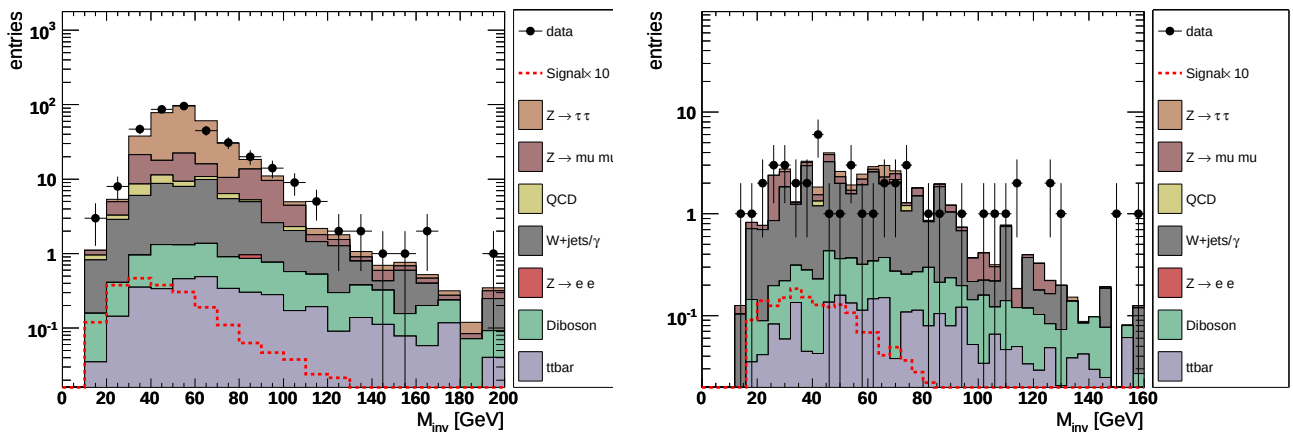

Figure 5.7: Distribution of the invariant mass after pre-selection (left) and after the minimal transverse cut (Cut 2) is applied (right) for $\mu + \tau_I$ final state. The expected signal, multiplied by a factor of 10, for a 160 GeV/c^2 SM Higgs is also shown.

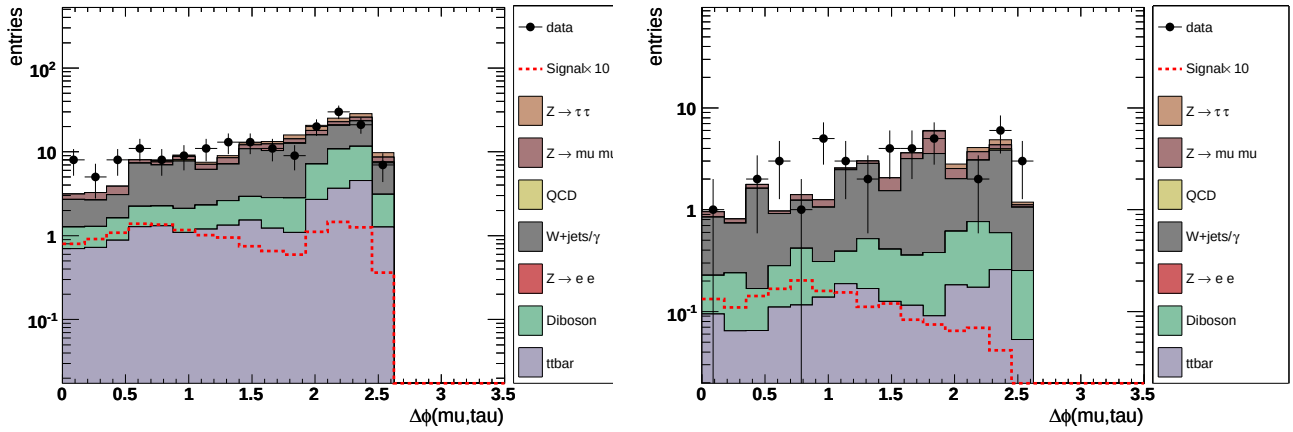

Figure 5.8: Distribution of the angle $\Delta\phi(\mu, \tau)$ after applying all cuts for the $\mu+\tau_{II}$ (left) and $\mu+\tau_I$ (right) final states. The expected signal, multiplied by a factor of 10, for a 160 GeV/c^2 SM Higgs is also shown.

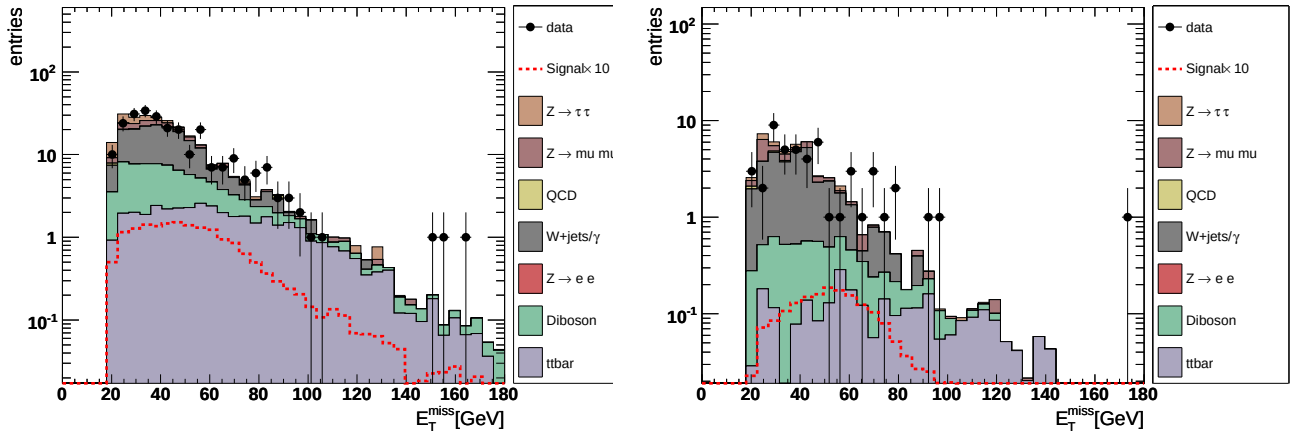

Figure 5.9: Distribution of the $\not\!\!E_{\mathrm{T}}$ after applying all cuts for $\mu + \tau_{II}$ (left) and $\mu + \tau_I$ (right) final states . The expected signal, multiplied by a factor of 10, for a 160 GeV/c^2 SM Higgs is also shown.

Selection	$m_H = 120$	$m_H = 140$	$m_H = 160$	$m_H = 180$	$m_H = 200$
pre-selection	0.94	1.68	2.40	1.57	1.11
$\not\!\!E_{\mathrm{T}}$	0.74	1.38	2.08	1.38	0.97
$M^T_{min}(\ell, \not\!\!E_{\mathrm{T}})$	0.49	1.09	1.77	1.20	0.82
$\Delta\phi(\mu, \tau)$	0.38	0.90	1.49	1.00	0.64

Table 5.3: Overview of expected signal yields for m_H =120-200 GeV/c^2 for $\mu + \tau_{II}$ selection.

infer that $\mu + \tau_{II}$ final state contributes more to the total signal than the $\mu + \tau_I$ final state. One can also see that the expected signal yield peaks at $m_H = 160$ GeV/c^2. qThe expected number of background events and the number of events observed in data at pre-selection and after applying successive selection cuts are given in Tables 5.5 and 5.6 for the $\mu + \tau_{II}$ and $\mu + \tau_I$ final states respectively. After applying all the selection criteria listed in the sec 5.9, the data is in good agreement with the SM expectations.

Selection	$m_H = 120$	$m_H = 140$	$m_H = 160$	$m_H = 180$	$m_H = 200$
pre-selection	0.09	0.15	0.22	0.15	0.10
$\not\!\!E_{\mathrm{T}}$	0.08	0.13	0.20	0.14	0.09
$M^T_{min}(\ell, \not\!\!E_{\mathrm{T}})$	0.05	0.11	0.18	0.13	0.08
$\Delta\phi(\mu, \tau)$	0.04	0.10	0.17	0.12	0.07

Table 5.4: Overview of expected signal yields for m_H =120-200 GeV/c^2 for $\mu + \tau_I$ selection.

Cut	Data	Sum Bkgd	$H_{160} \to WW$	$Z \to \tau\tau$
pre-selection	1993	2053	2.40	1392
$\not\!\!E_{\mathrm{T}}$	629	663	2.08	270
$M^T_{min}(\ell, \not\!\!E_{\mathrm{T}})$	254	257	1.77	26.81
$\Delta\phi(\mu, \tau)$	184	178	1.49	13.76

Cut	$W + jet/\gamma$	$t\bar{t}$	Diboson	$multijet$	$Z \to \mu\mu$
pre-selection	180.57	58.6	83.8	50.8	283.3
$\not\!\!E_{\mathrm{T}}$	144.76	53.1	63.6	3.6	126.32
$M^T_{min}(\ell, \not\!\!E_{\mathrm{T}})$	112.2	40.2	51.9	1.5	24.84
$\Delta\phi(\mu, \tau)$	88.2	24.6	32.42	0.90	18.23

Table 5.5: Number of expected background events and number of observed events, after successive selections with respect to $m_H = 160$ GeV/c^2 for $\mu + \tau_{II}$ final state. The statistical errors are small and hence neglected.

Cut	Data	Sum Bkgd	$H_{160} \to WW$	$Z \to \tau\tau$
pre-selection	375	354	0.22	224.72
$\not\!\!E_{\mathrm{T}}$	119	110	0.20	53.88
$M^{T}_{min}(\ell, \not\!\!E_{\mathrm{T}})$	49	46	0.18	2.7
$\Delta\phi(e, e)$	41	37	0.17	1.36

Cut	$W + jet/\gamma$	$t\bar{t}$	Diboson	$multijet$	$Z \to \mu\mu$
pre-selection	46.24	3.9	7.47	9.45	62.2
$\not\!\!E_{\mathrm{T}}$	34.57	3.58	6.17	1.08	11.45
$M^{T}_{min}(\ell, \not\!\!E_{\mathrm{T}})$	28.3	2.8	4.97	0.41	6.58
$\Delta\phi(e, e)$	24.1	1.94	3.98	0.14	5.87

Table 5.6: Number of expected background events and number of observed events, after successive selections with respect to $m_H = 160\ GeV/c^2$ for $\mu + \tau_I$ final state. The statistical errors are small and hence neglected.

5.10 Neural Networks

In order to further suppress the backgrounds surviving selection criteria presented in the section 5.5, multivariate techniques (Neural Networks) are used.

Neural Networks (NN) are a multivariate technique which is commonly used in high energy physics. They have been applied in RunI and RunII analysis at DØ [83] and are also used for and object identification techniques [82]. Inputs to the NN are variables that provide discrimination power between signal and background. The NN used in the analysis consists of three layers of "nodes", an "input layer", a "hidden layer" and an "output layer". A sigmoid function from the sum of the weighted input variables is calculated at each hidden node. The linear sum of these sigmoid functions appears at the output node. A NN is trained using samples of simulated signal and background events. During the training process, weights are adjusted at each node such that the signal is moved towards one and the background towards zero. A complete cycle of running through the entire training sample is called an "epoch". The complete training cycle used in this analysis has 600 epochs.

The NN used is the `TMultiLayerPerecptron` which is part of the `ROOT` package [84]. For training and testing of the NN, the MC samples are divided in orthogonal subsamples of equal size. A separate NN has been trained for each Higgs boson mass to be analyzed, training each time using all background samples and the corresponding signal sample. The NN has been re-trained for each Higgs mass using the events from $\mu + \tau_{II}$ final state only. The same NN has been used for $\mu + \tau_I$ final state.

5.10.1 NN Variable Selection

A list of variables sensitive to background and signal has been derived based on the separation power of the various distributions. Those variables can be divided into three classes, based on object kinematics, event kinematics and angular variables and are listed in in Table 5.7.

NN Analysis Variables	
Object kinematics	
p_T of muon	$p_T(\mu)$
p_T of tau	$p_T(tau)$
NN_τ output	
scalar sum of momenta of μ and τ	
Event Kinematics	
invariant mass of both leptons	$M_{\mathrm{inv}}(\mu,\tau)$
minimal transverse mass of one lepton and $\not\!\!E_{\mathrm{T}}$	M_T^{min}
missing transverse energy	$\not\!\!E_{\mathrm{T}}$
visible mass	$M_{\mathrm{inv}}(\mu,\tau) + \not\!\!E_{\mathrm{T}}$
Number of jets	
Scalar sum of p_T of jets	
Topological Variables	
angle between selected leptons	$\Delta\phi(\mu,\tau)$
angle between muon and $\not\!\!E_{\mathrm{T}}$	$\Delta\phi(\not\!\!E_{\mathrm{T}},\mu)$
angle between tau and $\not\!\!E_{\mathrm{T}}$	$\Delta\phi(\not\!\!E_{\mathrm{T}},\tau)$

Table 5.7: Input variables for the NN.

The relative importance of the input variables along with the background composition changes significantly over the analyzed mass range due to mass dependent kinematical characteristics of the expected signal.

Data/MC comparisons of the various input variables for $\mu + \tau_{II}$ final state are shown in Figs 5.10 - 5.15. The resulting NN output for a Higgs mass is displayed in Figs. 5.17 and 5.16 for the $\mu+\tau_I$ and $\mu+\tau_{II}$ final states respectively for a Higgs boson of mass m_H=160 GeV/c^2.

5.11 Limit Calculation

Since after all selection cuts the remaining candidate events are consistent with a background observation, limits on the production cross section times branching ratio $\sigma \times BR(H \rightarrow WW^* \rightarrow \mu\tau)$ are derived. The calculation is performed in the same way as already described in the sec 4.10 of the previous chapter of this thesis.

Since this is a feasibility study, with an aim to measure the sensitivity this final state can add to the already existing $H \rightarrow WW^* \rightarrow \ell^+\nu\ell^-\nu$ searches, a rather conservative approach of applying a flat 15% systematic to all the MC samples for background as well as signal is used.

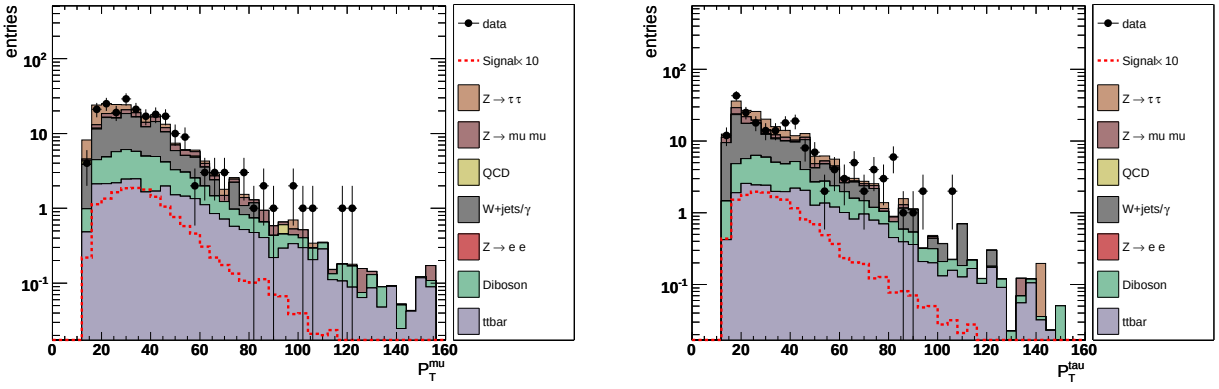

Figure 5.10: Distribution of the muon (left) and the tau p_T (right) as used in the NN. The signal as indicated by the red graph is representative for a Higgs boson mass of $m_{\mathrm{H}} = 160\ GeV/c$.

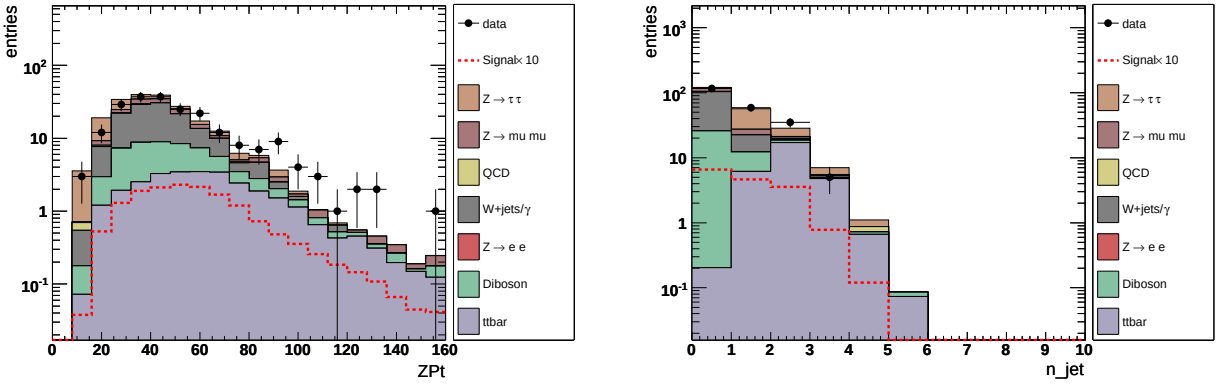

Figure 5.11: Distribution of the sum of Z p_T (left) and number of jets (right) as used in the NN.The signal as indicated by the red graph is representative for a Higgs boson mass of $m_H = 160\ GeV/c^2$.

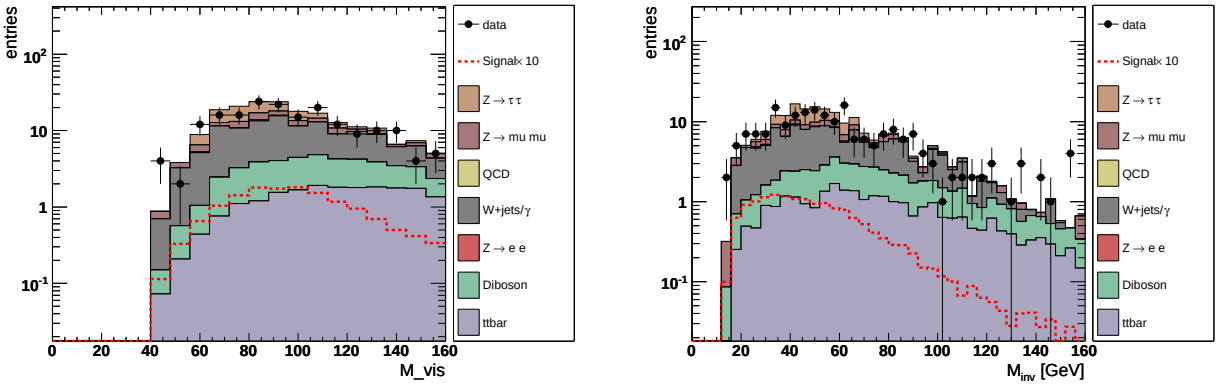

Figure 5.12: Distribution of the visible mass (left) and invariant mass (right) as used in the NN. The signal as indicated by the red graph is representative for a Higgs boson mass of $m_H = 160\ GeV/c$.

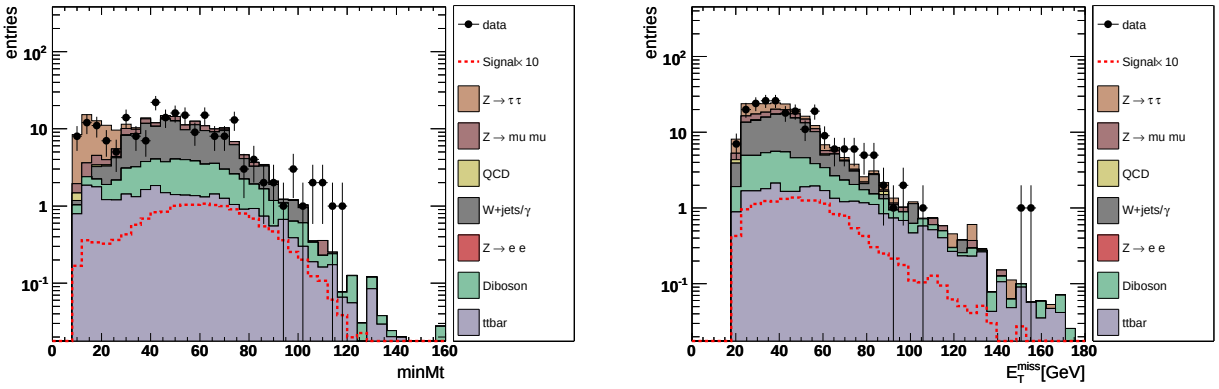

Figure 5.13: Distribution of the minimal transverse mass of the leptons (left) and of the missing transverse energy $M^T_{min}(\ell, \not{E}_T)$ (right) as used in the NN. The signal as indicated by the red graph is representative for a Higgs boson mass of $m_H = 160\ GeV/c^2$.

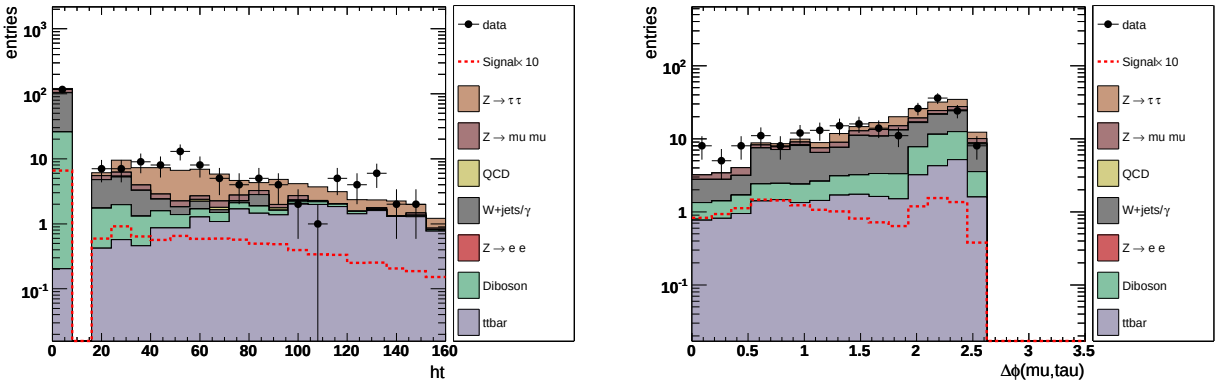

Figure 5.14: Distribution of the scalar sum p_T of jets (left) and $\Delta\phi(\mu, \tau)$ (right) as used in the Neural Network. The signal as indicated by the red graph is representative for a Higgs boson mass of $m_H = 160\ GeV/c^2$.

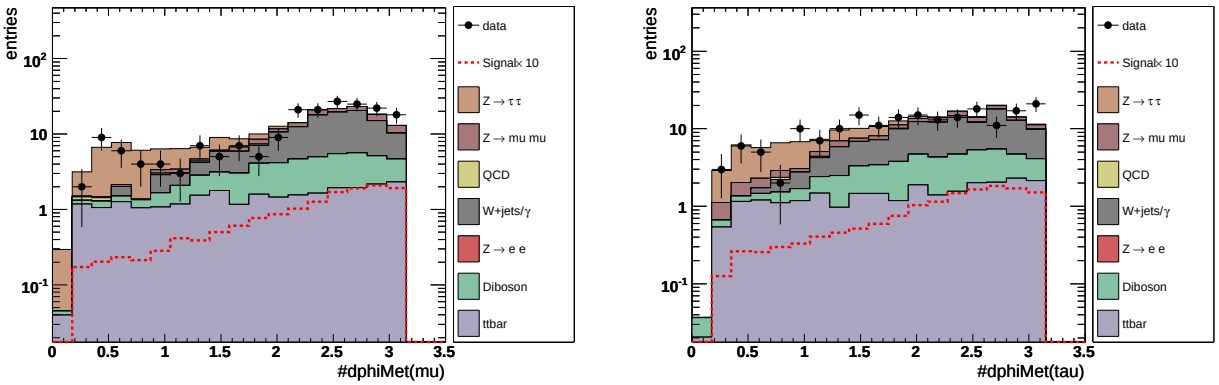

Figure 5.15: Distribution the opening angle between the muon (left) and tau (right) and $\not{E}_T$ as used in the Neural Network. The signal as indicated by the red graph is representative for a Higgs boson mass of $m_H = 160\ GeV/c^2$.

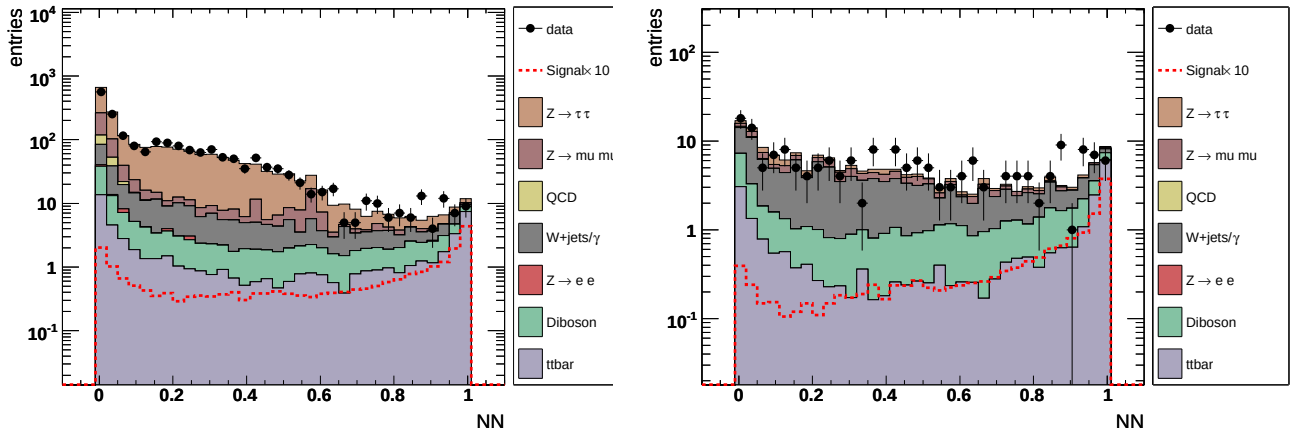

Figure 5.16: NN output for $m_H = 160\ GeV/c^2$ at pre-selection level (left) and after the $\Delta\phi(\mu,\tau)$ selection cut (right) for $\mu + \tau_{II}$

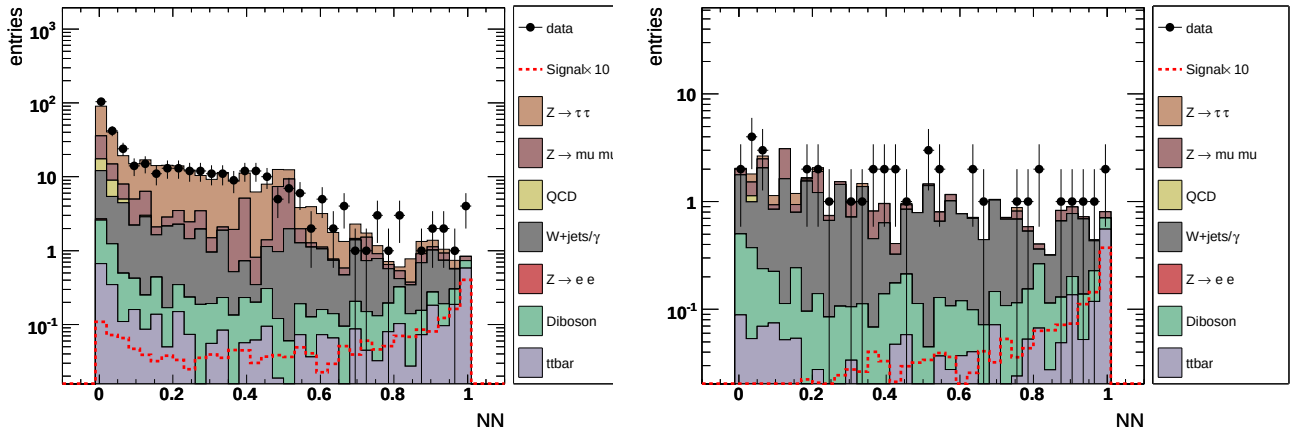

Figure 5.17: NN output for $m = 160\ GeV/c^2$ at pre-selection level (left) and after the $\Delta\phi(\mu,\tau)$ selection cut (right) for $\mu + \tau_I$

The limit is derived by using the shape of the NN output after the $\Delta\phi(\mu,\tau)$ cut for data, MC and the expected signal. Figs. 5.17 and 5.16 show the NN output for the $\mu + \tau_I$ and $\mu + \tau_{II}$ final states respectively for a Higgs boson of mass m_H=160 GeV/c^2. The expected and observed limits are shown in Fig. 5.18. The corresponding Log Likelihood Ratio (LLR) plot is shown in Fig. 5.19. In this plot the green and yellow shaded areas represent the $\pm1\sigma$ and $\pm2\sigma$ confidence levels for the "background-only" hypothesis and the black solid graph represent the observed limit. The "background-only" and "background + signal" hypothesis are given by the black and red dashed line respectively.

The expected limit at m_H=160 GeV/c^2 is 12.24 for the dominant $\mu\tau_{II}$ final state, while the expected limit of the more sensitive $H \rightarrow WW^* \rightarrow e^{\pm}\nu_e e^{\mp}\bar{\nu}_e$ final state (analysis already presented in this thesis) at m_H=160 GeV/c^2 is 1.92.

m_H [GeV]	115	120	125	130	135	140	145	150	155	160	165	170	175	180	185	190	195	200
	observed limit $\sigma \times BR(H \rightarrow WW^* \rightarrow \mu\tau)$ [$(\sigma \times$ BR)/SM]																	
$\mu\tau_{II}$	97.36	62.96	56.75	37.58	34.79	26.45	25.21	19.82	18.74	17.76	19.4	19.72	17.97	27.5	28.61	32.26	34.08	44.25
	expected limit $\sigma \times BR(H \rightarrow WW^* \rightarrow \mu\tau)$ [$(\sigma \times$ BR)/SM]																	
$\mu\tau_{II}$	60.31	56.05	39.623	29.72	23.56	22.14	17.59	15.73	14.48	12.24	12.44	13.69	14.88	18.26	19.38	22.46	24.38	30.36

Table 5.8: Observed and expected upper limits at 95% C.L. assuming 15 % systematics on all background as well as signal on the cross section times branching ratio for $\sigma \times BR(H \rightarrow WW^*)/SM$ for the $\mu\tau_{II}$ final states with respect to the SM expectation.

m_H [GeV]	115	120	125	130	135	140	145	150	155	160	165	170	175	180	185	190	195	200
	observed limit $\sigma \times BR(H \rightarrow WW^* \rightarrow \mu\tau)$ [$(\sigma \times$ BR)/SM]																	
$\mu\tau_I$	563.2	514.5	364.5	277.7	231.4	191.9	129.3	152.4	142.9	104.6	91.4	118.3	103.2	142.13	138.9	185.6	202.4	239.6
	expected limit $\sigma \times BR(H \rightarrow WW^* \rightarrow \mu\tau)$ [$(\sigma \times$ BR)/SM]																	
$\mu\tau_I$	452.31	323.33	257.39	180.64	141.46	129.41	105.37	91.61	76.99	58.65	63.03	71.9	73.55	90.93	93.50	112.51	126.79	154.68

Table 5.9: Observed and expected upper limits at 95% C.L. assuming 15 % systematics on all background as well as signal on the cross section times branching ratio for $\sigma \times BR(H \rightarrow WW^*)/SM$ for the $\mu\tau_I$ final states with respect to the SM expectation.

5.12 Future Outlook

A feasibility study was done in the $H \rightarrow WW^* \rightarrow \mu^{\pm}\nu_{\mu}\tau^{\mp}_{had}\bar{\nu}_{\tau}$ final state for 5 different SM Higgs boson masses. The sensitivity of this final state to the Higgs signal was found to be good. Hence a new analysis with improved methods was carried out. The new analysis with its methodology and techniques further improved the sensitivity of this final state [92]. This final state was then added to the Tevatron combination of SM Higgs boson searches in March 2011 [93].

.

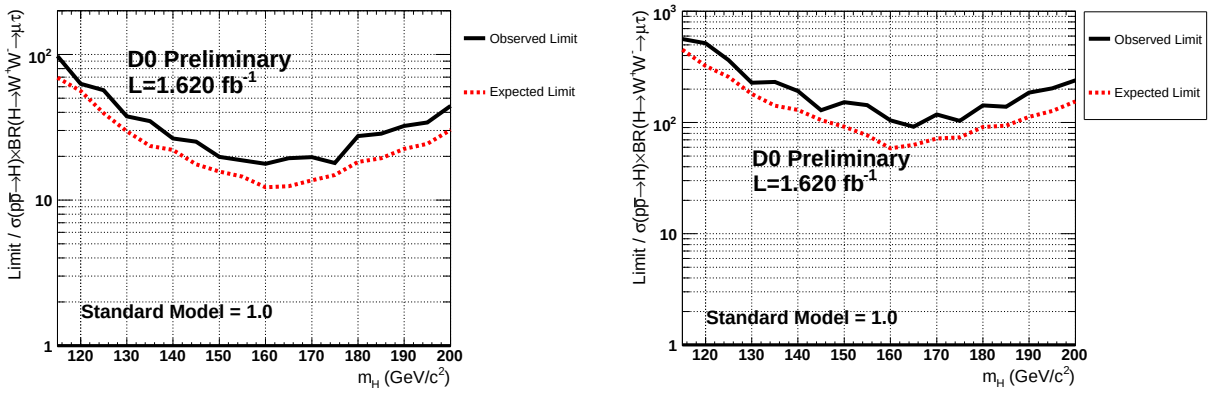

Figure 5.18: Expected and observed limits in terms of $\sigma \times BR(H \to WW^*) \times SM$ for the $\mu\tau_{II}$(left) and $\mu\tau_I$ (right) final state.

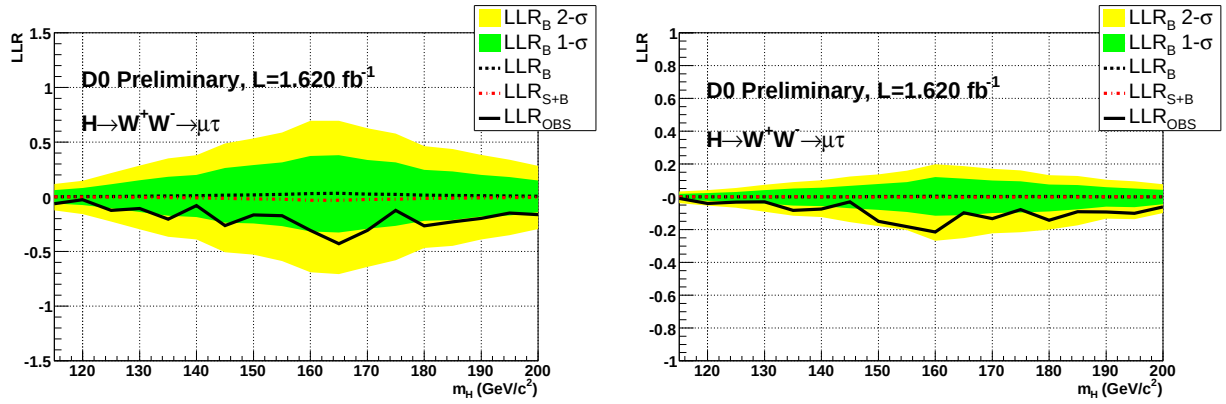

Figure 5.19: Log Likelihood Ratio for the expected and observed limit for $\mu\tau_{II}$ (left) and $\mu\tau_I$ (right)final state. The green and yellow shaded areas represent the $\pm 1\sigma$ and $\pm 2\sigma$ confidence levels for the background only hypothesis and the solid black graph represents the observed limit. The 'background-only' and 'background + signal' hypothesis are given by the black respectively the red dashed line.